Proof of Concept for Temperature and Strain Measurements With Fiber Bragg Gratings Embedded in Supercontainers Designed for Nuclear Waste Storage

Damien Kinet, Karima Chah, Andrei Gusarov, Alexey Faustov, Lou Areias, Ioannis Troullinos, Philippe Van Marcke, Bart Craeye, Eric Coppens, Didier Raymaekers, and Patrice Mégret, *Member, IEEE*

***Abstract*— The Belgian Agency for Radioactive Waste and Enriched Fissile Materials (ONDRAF/NIRAS) is developing a conceptual design for a supercontainer made of concrete and carbon steel for the post-conditioning of high-level nuclear waste prior to disposal in a geological repository site. This supercontainer should be instrumented to follow the temperature and strain evolution over time during and after the fabrication process. This paper shows that it is possible to embed bare fiber Bragg gratings in the supercontainer concrete to monitor *in situ* temperature and strain. The reason for choosing bare fibers, despite their known fragile nature, was to optimize the contact between the fibers and the concrete. Due to the simultaneous temperature and strain sensitivity of the fiber Bragg gratings, some sensors were also installed in a protective shielding consisting of plastic or aluminum to isolate them from effects of stress. This makes it also possible to extract both temperature and strain from the measured Bragg wavelength shifts. Moreover, the protective shielding also provides mechanical protection to avoid fiber breakage during concrete casting. The preliminary results of temperature closely agree with measurements obtained from thermocouples located near the fibers for validation purposes. Finally, the use of shielding in some of the fibers allowed to estimate strain levels in the concrete.**

***Index Terms*— Concrete buffer, fiber Bragg grating sensors, filler, heater, supercontainer concept.**

Manuscript received July 1, 2015; revised February 8, 2016 and March 17, 2016; accepted April 6, 2016. Date of current version June 21, 2016. P. Mégret is supported by the Belgian Science Policy IAP7/35 and Modern-2020 project of Horizon 2020 EU program. L. Areias acknowledges the EU FP7 Modern project for financial support.

D. Kinet, K. Chah, and P. Mégret are with the Electromagnetism and Telecommunication Department of the University of Mons, 7000 Mons, Belgium (e-mail: damien.kinet@umons.ac.be).

A. Gusarov is with the Belgian Nuclear Research Center, 2400 Mol, Belgium (e-mail: andrei.goussarov@sckcen.be).

A. Faustov is with Belgian Nuclear Research Center, Boeretang 200, Belgium (e-mail: afaustov@sckcen.be) and also with the Electromagnetism and Telecommunication Department of the University of Mons, 7000 Mons, Belgium.

L. Areias is with the European Underground Research Infrastructure for Disposal of Nuclear Waste In Clay Environment, 2400 Mol Belgium, and also with Mechanics of Materials and Constructions Department of the Vrije Universiteit Brussel, B-1050 Brussels, Belgium (e-mail: lou.areias@euridice.be).

I. Troullinos is with the European Underground Research Infrastructure for Disposal of Nuclear Waste In Clay Environment, 2400 Mol Belgium

P. Van Marcke, E. Coppens and D. Raymaekers are with the Belgian Agency for Radioactive Waste and Enriched Fissile Materials (ONDRAF/NIRAS), 1210 Bruxelles (e-mail: p.vanmarcke@nirond.be).

B. Craeye is with the University of Antwerp, EMIB Research Group on Energy & Materials in Infrastructure and Buildings, 2000 Antwerpen and also with the Odisee University College, DUBiT Research Unit, 9320 Aalst, Belgium (e-mail: bart.craeye@odisee.be).

Color versions of one or more of the figures in this paper are available online at http://ieeexplore.ieee.org.

Digital Object Identifier 10.1109/TNS.2016.2555337

I. Introduction

NUCLEAR power plants have been generating electricity for more than 50 years. In Belgium, 55% of the current supply comes from nuclear power. The long-term management of the nuclear waste generated by these activities — vitrified high level radioactive waste (VHLW) and spent fuel (SF) if declared as waste — remains an important challenge. ONDRAF/NIRAS considers geological disposal in poorly indurated clay as the reference solution for the long-term management of this waste. The disposal concept entails the post-conditioning of the waste in so-called supercontainers and the subsequent disposal of these packages in an underground repository.

The layout of a supercontainer (SC) containing a canister with vitrified high-level waste appears in Fig. 1 [1], [2]. It consists of an optional outer steel envelope, a concrete buffer, a filler and a water tight carbon steel overpack containing one or more waste canisters. The buffer has a diameter of 2.1 m, a height of 7 m and completely surrounds the overpack with a thickness varying between 54 cm and 75 cm, depending on the waste contained in the SC. The construction of a SC would consist of four main stages, as shown in Fig. 2.

One of the long-term functions of the concrete buffer is to provide and buffer a high alkaline chemical environment that favors the formation of a tightly adhering passive oxide film on the external surface of the carbon steel overpack, which protects the underlying metal and is believed to result in very low and uniform corrosion rates [3].

The long-term safety function of the overpack is to contain the radionuclides during the thermal phase. This is the phase during which the host rock around the disposed waste is at an elevated temperature due to the heat generated by the high level waste. The thermal phase will last several thousands of years.

To investigate the feasibility of the SC concept at large scale, two half-scale tests have been performed. 'Half-scale' refers

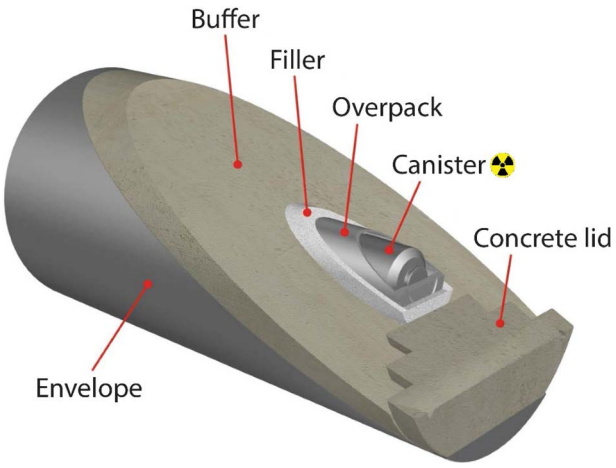

Fig. 1. Belgian supercontainer concept.

Fig. 2. Main construction phases of the supercontainer. From left to right: construction of the buffer and outer envelope, insertion of the overpack, casting of the filler and installation of lid.

TABLE I
AVERAGE FRESH PROPERTIES OF BUFFER AND FILLER FINAL MIXES.

Property	Buffer	Filler
Slump flow [mm]	703	641
V-Funnel [s]	21.3	3.3
Density [kg m^{-3}]	2384	2240
Water content[kg m^{-3}]	195.7	261.0
Water/Cement ratio	0.5	1.0

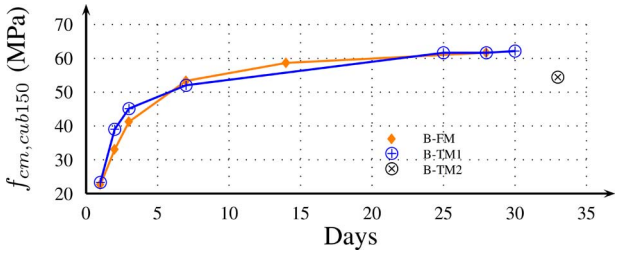

Fig. 3. Compressive strength of SCC buffer trial [TM] and final [FM] mixes.

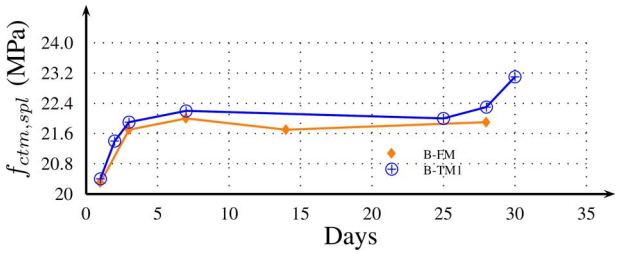

Fig. 4. Splitting tensile strength of SCC buffer trial [TM] and final [FM] mixes.

to the size of the test mockup, which has approximately a true diameter (2.1 m) but half of the height of a real SC (reduced height was 3.5 m). The first half-scale, performed in 2009, demonstrated to a far extent that the SC can be constructed using available industrial techniques. One of the objectives of the second half-scale test, carried out in 2014, was to further investigate the feasibility of constructing the SC and to advance our understanding of the thermo-mechanical behavior of the concrete materials. To this end, various sensors were installed on the SC. Among them, optical fibers with three fiber Bragg gratings (FBG) in cascade were embedded into the concrete during the fabrication process at various locations to make *in situ* monitoring. The obvious advantage of FBGs is their multiplexing capabilities, allowing to put many gratings in the same fiber and making thus a very simple multipoint measurement system. The principal drawback is the fragility of the fibers especially during the casting of the concrete.

This paper shows that fibers can be embedded into concrete in real industrial conditions, and that from wavelength shifts of FBG measurements, temperature and strain can be recovered.

II. CONCRETE PHYSICAL PROPERTIES

The buffer is a non-reinforced self compacting concrete (SCC) made using ordinary Portland cement, limestone powder and aggregates and a water/cement ratio of 0.5 [4]. On the other hand, the filler consists of a cement mortar with smaller size aggregate composition and a water/cement ratio of 1.0.

An overview of the fresh properties obtained for the final mixes of both the (SCC) buffer and the filler appear in Table I. All the samples were hardened under ideal environmental conditions of 20 °C and 90% relative humidity. The targeted fresh properties of the buffer and filler materials were determined in the laboratory prior to the start of the half-scale testing program. The mortar used in the filler was designed with one main objective: namely, to provide a homogeneous material with a high degree of fluidity to easily fill the gap left between the overpack and the buffer. For practical reasons, the same mortar was used to close the lid. Fig. 3 shows the evolution of compressive strength of the SCC for both trial (B TM1 and 2) and final (B FM) mixes. The trial mixes were prepared a few weeks before the test. The compressive strength $f_{cm,cub150}$ was determined using 15 cm cubic samples of different curing ages, varying between 1 day and 33 days, as a mean value of at least three uniaxial tests for each age. As observed, the results for both the trial and final mixes are very similar.

Similar results showing the evolution of tensile strength of the buffer appear in Fig. 4. The splitting tensile strengths $f_{ctm,spl}$ of B-TM1 and B-FM were determined for different ages, varying between 1 day and 30 days, as a mean value of at least three prisms for each age. The results for the trial and final mixes are quite similar.

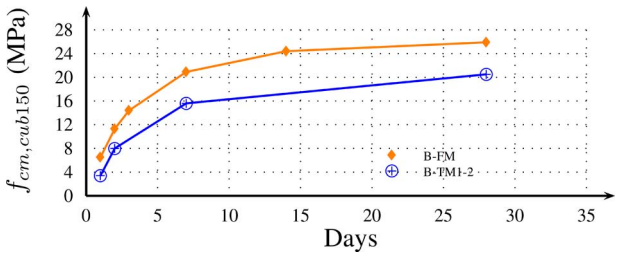

Fig. 5. Compressive strength of filler trial [TM] and final [FM] mixes.

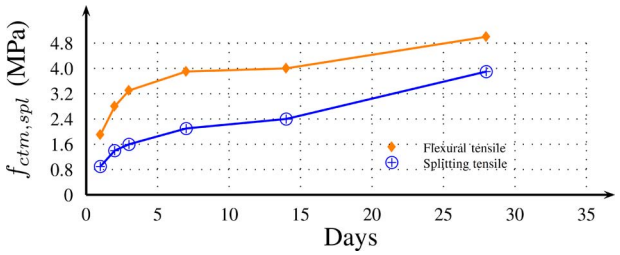

Fig. 6. Flexural and splitting tensile strengths of the filler final mix.

TABLE II
TIME SCHEDULE

Phase	Day	Milestone
Phase 1	0	Cast concrete buffer
	6	Removal inner mould
	29	Removal outer mould
Phase 2	56	Cast filler & start heating
Phase 3	133	Shut OFF heater & start cooling phase
	167	END of test

Fig. 7. View of setup during installation showing assembled mould for the casting of the concrete buffer.

Measured values of compressive and tensile strengths obtained for the filler appear in Figs. 5 and 6, respectively. The compressive strength varies between 3.4 and 20.5 MPa for the trial mix (TM) and 6.5 to 25.9 MPa for the final mix (FM) batches. The tensile strength of the filler was measured only for the final mix. The results obtained using both flexural and splitting methods show values of tensile strength varying between 1.9 and 5.0 MPa and 0.9 and 3.9 MPa , respectively.

III. SETUP OF THE SECOND HALF-SCALE TEST

The half-scale tests (Fig. 7) consist of three main phases depicted in Table II. Phase 1 is the construction of the concrete buffer. Phase 2 is a heating phase that includes the installation of a heated overpack, the filling of the gap between the overpack and the buffer, and the closing of the space occupied by the lid, all with a cement mortar. Phase 3 is a cool down period following the shutdown of the heating phase.

The overpack is a carbon steel cylindrical container with a diameter of 508 mm and a thickness of 16 mm . It contains four heating elements to simulate the heat generated by the radioactive waste. The heating elements are buried in dry, clean sand for good thermal conductivity and produce a homogeneous heat distribution at a constant power of 300 W/m.

A layer of 8 cm thickness Rockwool kept the outside of the mockup insulated for the duration of the test to help reducing both temperature losses as well as thermal gradients in the concrete buffer and filler. After removal of the inner mould, the top of the inner cavity was covered to prevent desiccation. To enhance the curing process, the inner cavity was kept moist by regularly spraying water during the first 28 days of the test.

In the first half-scale test [2] a number of parameters were monitored including temperature, ambient wind velocity, displacement and deformation, whereas in the second half-scale test more extensive monitoring sensors were incorporated, as displayed in Table III. This second test incorporated several types of monitoring devices including Digital Image Correlation (DIC), Acoustic Emission (AE), Ultrasonic Pulse Velocity (UPV), corrosion sensing techniques and optical fibers with and without fiber Bragg gratings (FBGs) [1], [3], [5]–[7]. Seven fibers with FBGs were embedded in the concrete buffer during the casting and curing of the concrete in phase 1 and eight additional fibers with sensors were embedded in the filler during phase 2.

IV. FIBER BRAGG GRATING SENSORS

The FBGs were written into hydrogenated standard singlemode optical fibers by means of a double-frequency Argon laser emitting at 244 nm by the Lloyd mirror set-up [8], [9] (Fig. 8). This scheme made it possible to write

TABLE III
MONITORING PARAMETERS IN SECOND HALF-SCALE TEST

Parameter	Sensor test 1	Sensor test 2
Temperature	Thermocouples	Thermocouples and FBG
Displacement	LVDT (Linear Variable Displacement Transducer)	LVDT
Strain	Strain gauges (including vibrating wire gauges)	Strain gauges and FBG
Wind velocity	Anemometers	Anemometer
Relative moisture		Humidity TDR probes
Onset and evolution of cracking		DIC (Digital Image correlation)
Crack detection and evolution		Acoustic Emission (AE)
Total pressure		Pressure sensors
Oxygen flux, corrosion potential, active corrosion rate		Corrosion sensors

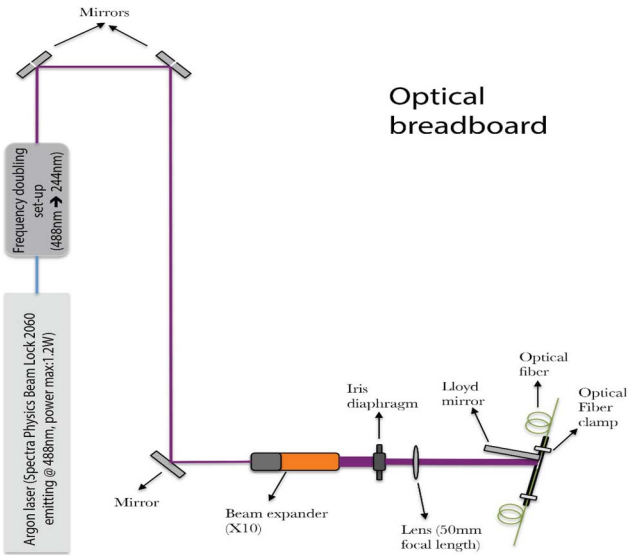

Fig. 8. General view of our photoinscription set up [9].

FBGs at different Bragg wavelengths by changing the angle of the mirror with respect to the laser beam. The cylindrical lens (50 mm focal length) allows focusing the beam on the optical fiber. Due to UV absorption in the fiber protective polymer coating, it is necessary to remove the coating before FBG inscription. The gratings were annealed at 100 °C for 24 h to stabilize them and to eliminate the hydrogen. Moreover, they were not recoated after the fabrication. The FBGs have a length of 4 mm and are of type I.

In the SC half-scale test some of the FBGs were embedded in the concrete without packaging, while others were protected with a plastic tube (inner diameter of 0.5 mm and thickness of 0.2 mm) or with an aluminum tube (inner diameter of 1.5 mm and thickness of 0.7 mm). At the exit point of the fibers, aluminum tubes were used to protect the fibers against

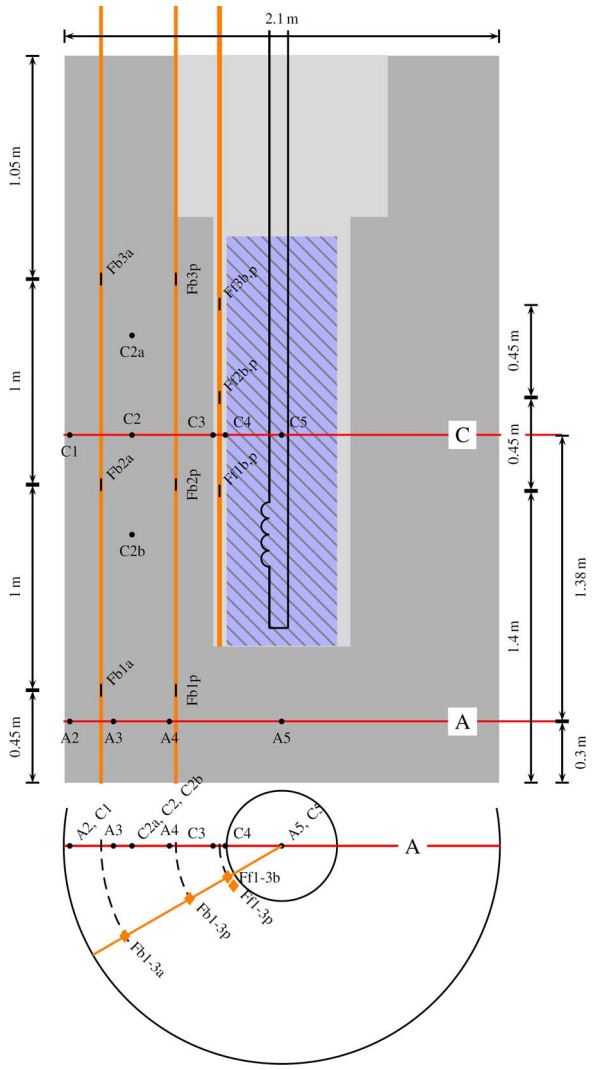

Fig. 9. Approximate positions of the FBGs (-) and thermocouples (•): buffer in gray, filler in light gray and heater in hatched blue. Fb1a to Fb3a are located in aluminum tube embedded in the buffer, Fb1p to Fb3p are in plastic tube embedded in the buffer, Ff1b to Ff3b are bare FBGs embedded in the filler, and Ff1p to Ff3p are FBGs in plastic tube embedded in the filler. A2 to A5, and C1 to C5 are thermocouples at level A and C respectively.

breakage. From a mechanical point of view, plastic tube are more flexible and easier to handle than aluminum tubing.

Fig. 9 shows that the locations of the thermocouples (TC) are in a vertical plane whereas the fiber Bragg grating sensors (FBG) used in this experiment are in another vertical plane making an angle of 30° with the thermocouples plane. As the symmetry is cylindrical, this geometry is expected to be equivalent to that with thermocouples and fiber sensors in the same vertical plane. This approximation is better for level C than for level A during the heating phase. Fb1p to Fb3p are located in plastic tube whereas Fb1a to Fb3a are placed inside aluminum tube. All these FBGs were embedded in the buffer during the first phase of the test. TCA2 to TCA5, and TCC1 to TCC5 denote thermocouples located at the level A and level C, respectively. During the second phase, bare FBGs (Ff1b to Ff3b) and FBGs in plastic tube (Ff1p to Ff3p) where embedded in the filler in the space between the buffer and the overpack.

FBGs in aluminum tube are free to move inside the tube, which is rigid and not deformed during the casting of the concrete. These FBGs will thus be only sensitive to temperature and their readings can be directly compared with those obtained from thermocouples located nearby. On the other hand, FBGs directly embedded into the concrete will be sensitive to both temperature and stress inside the concrete. They can be used to estimate the strain as the temperature is known from the FBGs in aluminum tube.

Indeed, the Bragg wavelength shift $\Delta\lambda_i$ of the i^{th} FBG is a function of the temperature T and the strain ϵ according to the relation:

$$\Delta\lambda_i = K_{Ti}T + K_{\epsilon i}\epsilon \tag{1}$$

where K_{Ti} and $K_{\epsilon i}$ are calibration coefficients determined before the experiment [10]. If we use FBG1 from the aluminum tube and FBG2 from the bare FBGs, (1) leads to:

$$\Delta\lambda_1 = K_{T1}T \tag{2}$$

$$\Delta\lambda_2 = K_{T2}T + K_{\epsilon 2}\epsilon \tag{3}$$

as FBG1 is isolated from stress. Provided that FBG1 and 2 are close enough to be at the same temperature, temperature is computed from (2), and (3) gives the strain.

For the FBGs in plastic tube, the situation is more complicated as the tube can be deformed during the casting of the concrete leading to constrained fiber movements inside the tube. This can lead to some dependency on stress. In that case, (1) will lead to two equations with two unknowns that can be inverted provided that the determinant of the system is not null. In practice, in a first approximation, we will neglect the deformation of the plastic tube and use the same procedure as with the aluminum tube to retrieve the strain inside the filler.

The monitoring performed using FBGs was limited to the test periods in phase 1 between days 6 and 29, and in phase 2 from days 56 to 70 (Table II). For the monitoring in phase 1, a series of 7 optical fiber sensors were fixed to the bottom and top of the outer mould (Fig. 10), while the spacers shown kept the optical fibers in place during casting.

Before installing the overpack with its heater for the start of phase 2, a series of 8 optical fibers were installed in the filler at a distance of 5 cm from the overpack (Fig. 11).

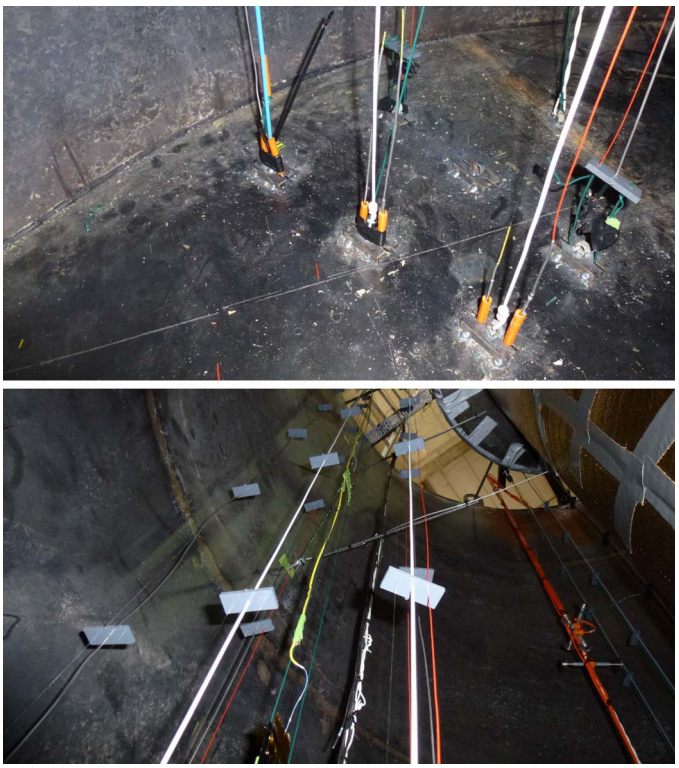

Fig. 10. (Top) fixing of optical sensors to the floor of the mould; (Bottom) guide spacers used to align the optical fibers.

Fig. 11. (Left): Optical fibers with and without protection tubes placed directly on the overpack or right next thanks to spacers and a tensioner; (Right): Casting of the filler.

V. Results

A. Evolution of Bragg Wavelength Inside the Buffer

Due to fiber breakages and/or excessive bending, caused either during casting or while removing the internal mould, only two optical fibers originally embedded in the concrete buffer (Phase 1) were fully exploited, one in an aluminum tube and the other in a plastic tube. Moreover, these sensors were monitored only during limited periods. Fig. 12 shows the evolution of the Bragg wavelength of Fb1p sensor, packaged in a plastic tube and embedded in the buffer, capturing the main events of the SC construction.

B. FBG Sensors in the Aluminum Tubes Inside the Buffer

Using the measured Bragg wavelength shift, it is possible to calculate the temperature evolution from relation (2) in the buffer during curing in Phase 1 and the first days of the heating Phase 2 (Fig. 13). The sensitivity value K_T, based on a calibration test, was 10.48 pm/°C. The figure also shows the reference temperature measurements obtained

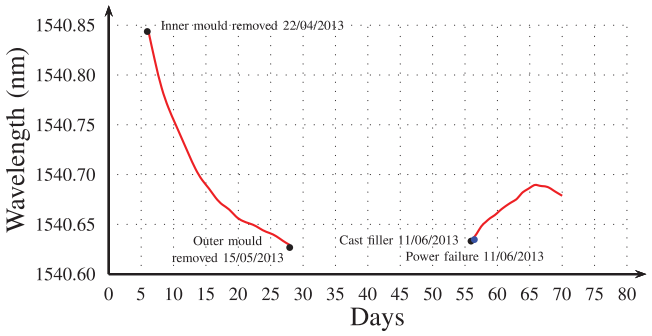

Fig. 12. Bragg wavelength evolution of the Fb1p inside the plastic tube embedded in the buffer.

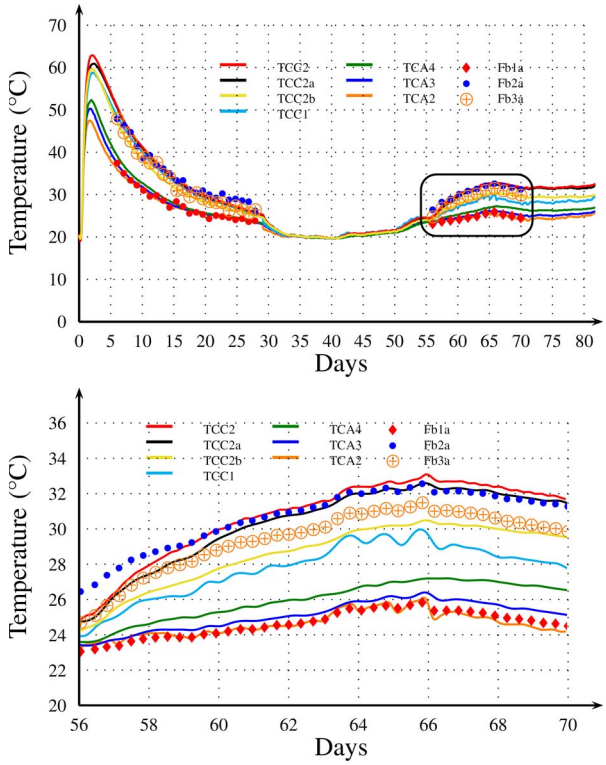

Fig. 13. (Top) Temperature evolution in the buffer from Fb1–3a and reference thermocouples from start of Phase 1; (Bottom) zoom in on the start of the heat phase. Start of heating Phase 2 = 56 days. (Plain curves are labeled from top to bottom at day 70).

with thermocouples located near the optical sensors, showing a good match between the two methods.

To better explain the results, Fig. 14 shows the temperature profiles for levels A and C obtained from the thermocouples TCA2 to TCA5, and TCC1 to TCC3, respectively at day 66. Similar profiles can be extracted for all the days and will show the same trends but with different gradient values.

The temperature measurement from Fb1a is between the temperature given by the thermocouples TCA2 and TCA3, as expected from the FBG location. Moreover, Fig. 14 shows that the temperature variation is radially linear with a gradient of -2.9 °C/m. Therefore, Fb1a, TCA4 and TCA3 should agree very well, as it is indeed the case.

For Fb2a, although it is located nearly mid-way between TCC1 and TCC2, the temperature is above TCC2 till day 60,

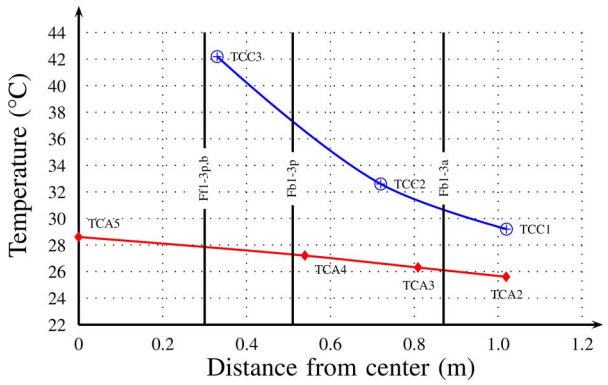

Fig. 14. Temperature versus radial distance at day 66 for levels A and C. Radial positions of the FBGs are also on the graph to make easier comparisons with TC.

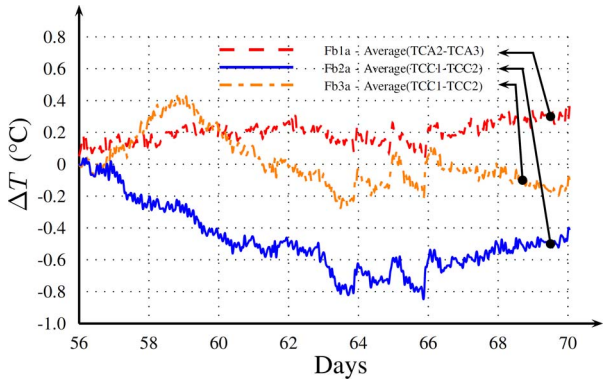

Fig. 15. Temperature difference in the buffer between Fb1–3a and reference thermocouples.

roughly equivalent to that of TCC2 from days 60 to 64 and then below TCC2. As shown in Fig. 14, the temperature profile is not linear and the gradient between TCC2 and TCC1 is -11.3 °C/m.

Fig. 15 shows the difference in temperature measured by the FBGs and the average temperature values obtained by averaging thermocouples bracketing the FBGs. As shown, this difference is less than ± 1 °C. From these results, it is confirmed that FBGs installed inside aluminum tubes are only sensitive to temperature since the FBGs are totally free to move in the tube.

C. FBG Sensors Installed in Plastic Tubing Inside the Buffer

Fig. 16 shows the difference in temperature measured between Fb1-3p and that obtained with reference thermocouples TCC2, TCC2a, TCC3 and TCA4 located nearest to the optical fiber sensors. As shown in Fig. 14, the temperature profile is linear at level A with a gradient of -2.9 °C/m and exponential-like at level C with a gradient of -24.6 °C/m between TCC2 and TCC3. So we have taken day 56 as the reference point and we have compared Fb1p with TCA4, Fb2p with the average of TCC2 and TCC3, and Fb3p with TCC2a.

As shown, the temperature differences range between 2 °C and 4 °C. These relatively large differences can be explained by the fact that the FBGs and the thermocouples are not

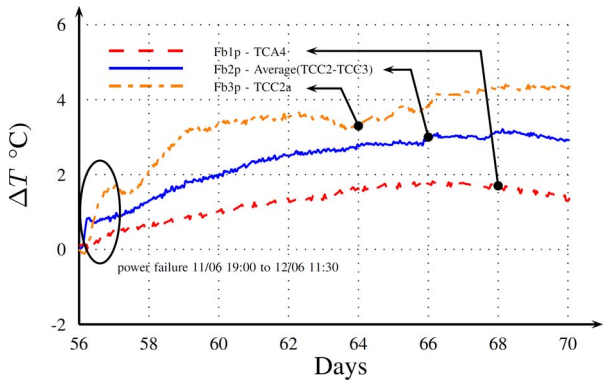

Fig. 16. Temperature difference in the buffer between Fb1–3p installed in plastic tubing and reference thermocouples.

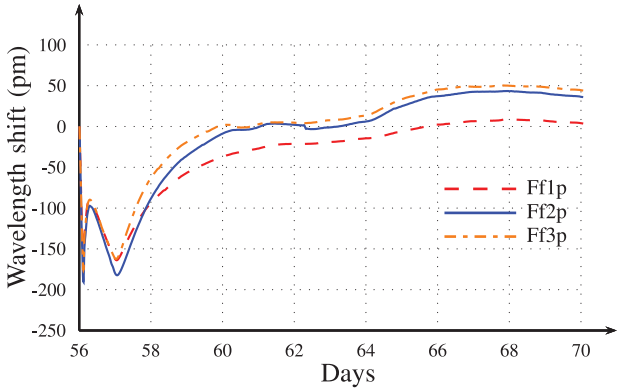

Fig. 17. Bragg wavelength during Phase 2 for Ff1–3p protected in plastic tubes embedded in the filler.

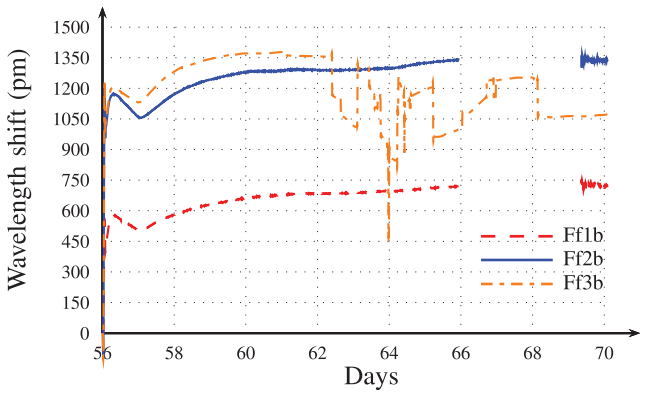

Fig. 18. Bragg wavelength during Phase 2 for bare gratings Ff1–3b embedded in the filler.

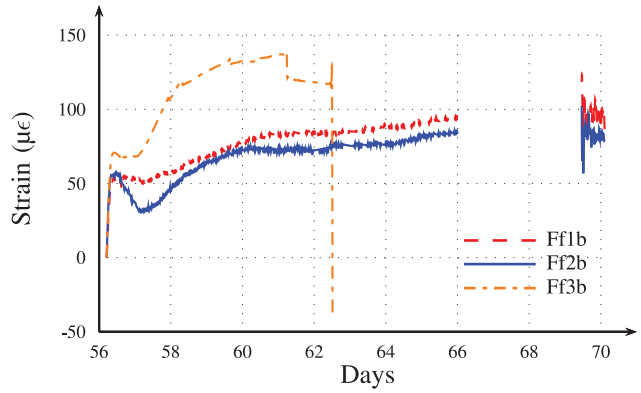

Fig. 19. Estimated values of axial strain registered by the bare gratings Ff1–3b in the filler during Phase 2.

located exactly at the same place. For example, the lower curve, which shows the smallest difference of 2 °C for the three sensors, also corresponds to shortest distance between the sensor Fb1p and the reference thermocouple TCA4 (Fig. 9). Moreover, these measurements are located at level A where the temperature profile is linear with a small gradient. The other two FBGs (Fb2p and Fb3p, upper curves) are located farther away from the reference thermocouples TCC2, TCC2a and TCC3 and are subject to an exponential-like temperature profile with a high gradient. In addition, these two FBGs are closest to the heater, which further contributes to the observed higher temperature differences. It also explains why the effect of the power failure is the first to appear for Fb2p, which lies at the mid height of the mock up where the temperature is the highest.

D. FBG Sensors Embedded in the Filler

Thanks to results of phase 1, fiber samples preparation has been improved and only one fiber out of eight died during phase 2.

Fig. 17 shows the evolution of the Bragg wavelength for the Ff1–3p packaged in the plastic tubes in the filler. As these FBGs are mainly sensitive to temperature, the results clearly show a sharp drop in temperature a few hours after the start of the heat phase, caused by a general power failure. The power to the heater was reestablished on day 57, as shown.

Fig. 18 presents the Bragg wavelengths for the bare gratings Ff1–3b located in the filler and close to Ff1–3p (see Fig. 9). The gaps in the data from day 66 to day 69 for Ff1b and Ff2b located in the lower and middle section of the heater result from the inability to differentiate the measurable spectrum from the background signal, which is needed to determine the FBG wavelength. The measurements for Ff3b, located near the top of the SC, stopped earlier, in day 62, and then shows an erratic behavior.

The evolution of strain calculated from the wavelength measurements appears in Fig. 19 and is calculated according to the procedure described in [10] and outlined in Section IV. It shows a dilatation for both Ff1b and Ff2b until the data gaps on day 66, followed by an abrupt drop on day 69, after resuming monitoring for both FBGs. Due to the gaps in the data, it is not possible to identify the start of the observed drops in strain.

In the case of Ff3b, the Bragg shift increases rapidly on day 57, coinciding with the re-start of the heater after the power failure. The curve provides indications of strain release, displayed by small and sudden drops in the wavelength, and a tendency to flatten out before the last usable measurement was made on day 61. The shape and associated features displayed by the curve suggest the development of cracks in the filler.

The results of acoustic emission (AE) measurements in Fig. 20, showing the cumulative AE events registered in Phase 2, provide another evidence of crack initiation in

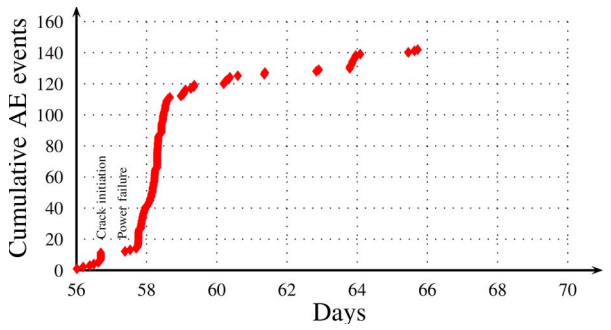

Fig. 20. Cumulative AE events showing initiation of cracking approximately 1 day after the start of heating Phase 2. [5].

the SC mockup [5]. In particular, the results indicate the initiation of cracking at approximately the same time as the events in Ff3b. Further analysis is underway to elucidate the cracking phenomena observed in the SC mockup.

VI. Conclusions

This paper presents results of temperature and strain measurements obtained using both bare and packaged FBG sensors embedded in concrete during a recent half-scale test of the Belgian supercontainer concept.

The measurements of temperature obtained in this study using optical fiber Bragg sensors closely agree with reference measurements made using classical thermocouples. Moreover, strain estimation was realized and some correlation with acoustic emission analysis was possible indicating crack formation in the concrete. All these results confirm the suitability of embedded optical fibers to monitor temperature and strain in the SC mock up. In particular, the bare fibers offered the best sensitivity over shielded ones to measure deformation and to identify potential cracking in the concrete.

The fragile nature of the optical fibers, especially those used without protective shields, coupled with a general lack of experience in the installation of these fibers in concrete, resulted in a relatively high number of breakages both during installation and monitoring (9 fibers out of 15 survived). Additional efforts should be made in future installations to improve the survival rate of the fibers. These could include:

- Better embedding and fixing techniques both in and out of the concrete;
- Higher protection of bare FBGs using aluminum tubing with open windows allowing a direct contact of the concrete with the optical fiber sensors;
- Improved protection of the optical fibers between two successive FBGs;
- Use of more rigid plastic tubes to reduce stress sensitivity;
- Use of softer plastic tubes to enhanced stress sensitivity and avoid bare fibers.

Finally, the results of the second half-scale test confirm those of the first one carried out in 2009 concerning the construction feasibility of the SC. Both provide sufficient confidence that the SC can be constructed using current industrial techniques. The second test, however contains a more extensive and innovative monitoring installation, thereby contributing to a better understanding of construction feasibility issues including the mechanisms of potential cracking of the concrete, corrosion and overall performance of the supercontainer, ... Since the cabling for electrical sensors is much more complex and intrusive than those used in optical fibers, (one fiber can handle 10–20 sensors or more), the use of optical technologies is expected to grow in monitoring applications for future radioactive waste repositories.

Acknowledgment

The authors acknowledge the technical help provided by C. Lefèvre (ESV EURIDICE) for installation of the sensors.

References

[1] L. Areias, S. Iliopoulos, L. Pyl, and J. Gu, "Recent experience with the use of DIC and AE monitor surface cracking in a cylindrical concrete buffer," in *Proc. Implementing Geological Disposal Technol. Platform IGD-TP EF4, Workshop (Monitoring)*, 2013.

[2] L. Areias, B. Craeye, G. De Schutter, H. Van Humbeeck, W. Wacquier, L. Villers, and A. Van Cotthem, "Half-scale test: an important step to demonstrate the feasibility of the belgian supercontainer concept for disposal of HLW," in *Proc. 13th Int. Conf. Environ. Remediation Radioactive Waste Mngmnt*, 2010.

[3] B. Kursten, F. Druyts, L. Areias, Y. van Ingelgem, D. De Wilde, G. Nieubourg, G. S. Duffó, and C. Bataillon, "Preliminary results of corrosion monitoring studies of carbon steel overpack exposed to supercontainer concrete buffer," *Corrosion Eng., Sci. Technol.*, vol. 49, no. 6, pp. 485–491, 2014.

[4] B. Craeye, *Early-age Behaviour of Concrete Supercontainers for Rad-waste Disposal*, Ph.D. dissertation dissertation, Ghent University, Ghent, 2010.

[5] S. Iliopoulos, D. Aggelis, L. Pyl, J. Vantomme, P. Van Marcke, E. Coppens, and L. Areias, "Detection and evaluation of cracks in the concrete buffer of the Belgian nuclear waste container using combined NDT techniques," *Construct. Building Mater.*, vol. 78, pp. 369–378, 2015.

[6] T. Geernaert, S. Sulejmani, C. Sonnenfeld, G. Luyckx, K. Chah, L. Areias, P. Mergo, W. Urbanczyk, P. Van Marcke, E. Coppens, H. Thienpont, and F. Berghmans, "Microstructured optical fiber Bragg grating-based strain and temperature sensing in the concrete buffer of the Belgian supercontainer concept," in *Proc. 23rd SPIE Int. Conf. Opt. Fiber Sensors*, 2014, vol. 9157. pp. 915777-1–4.

[7] B. Craeye, G. De Schutter, W. Wacquier, H. Van Humbeeck, A. Van Cotthem, and L. Areias, "Closure of the concrete supercontainer in hot cell under thermal load," *Nucl. Eng. Design*, vol. 241, pp. 1352–1359, 2011.

[8] R. Kashyap, *Fiber Bragg Gratings*, 2nd ed. Cambridge: Academic Press, 2009.

[9] D. Kinet, *Utilisation de capteurs à réseaux de Bragg fibrés pour le suivi de matériaux composites pendant et après fabrication*, Ph.D. dissertation dissertation, University of Mons, 2014.

[10] D. Kinet, P. Mégret, K. Goossen, L. Qiu, D. Heider, and C. Caucheteur, "Fiber Bragg grating sensors toward structural health monitoring in composite materials: Challenges and solutions," *Sensors*, vol. 14, pp. 7394–7419, 2014.